Convection in a rotating, horizontal cylinder with radial and normal gravity forces

By FOLUSO LADEINDE† AND K. E. TORRANCE

Sibley School of Mechanical and Aerospace Engineering, Upson Hall, Cornell University, Ithaca, NY 14853, USA

Convection driven by radial and normal gravity forces in a rotating, horizontal cylinder is examined. The cylinder is subjected to uniform volumetric heating and constant-temperature wall cooling. The parameters are the radial-gravity and normal-gravity Rayleigh numbers, Ra_r and Ra_g (with Ra_r, $Ra_g \leqslant 10^6$), the rotational Reynolds number, $Re = 2\Omega\, r_0^2/\nu$ ($0 \leqslant Re \leqslant 250$), and the Prandtl number ($Pr = 7$). Critical conditions for the radial-gravity rest state correspond to a two-cell flow in the azimuthal plane with $Ra_{r,c} = 13\,738$. Finite-amplitude transient and steady flows are obtained with a Galerkin finite element method for Rayleigh number ratios in the range $0.1 \leqslant Ra_r/Ra_g \leqslant 100$. When radial gravity dominates the flows tend to be multicellular and, during transients, initial high-wavenumber forms evolve to lower-wavenumber forms. When normal gravity dominates the flows are bicellular. When radial and normal gravity forces are comparable, in the presence of rotation, complex time-dependent motions occur and the largest rates of fluid circulation and heat transfer are observed.

1. Introduction

In this paper we examine convection driven by radial and normal gravity forces in a horizontal cylinder rotating about its axis. The radial gravity can be a result of centrifugal effects or self-gravitation. The normal gravity is due to an external (vertical) gravity field. Applications include food processing and crystal growth (Yang, Yang & Lloyd 1988). Further, some of the observed flows resemble those in model problems in astrophysical/planetary fluid dynamics (Hide & Mason 1970; Hsui, Turcotte & Torrance 1972; Weir 1976).

A principal motivation for the present study comes from the food industry, where canned liquids are often thermally processed (sterilized or pasteurized) while rotating and moving on a conveyor belt (Lopez 1981; Ladeinde 1986). The kinematic motion can be complex, but a major component frequently involves axial rotation of a horizontal can. After rotation is established, a can is subjected to transient heating and cooling. Buoyancy-driven convection, caused by rotation and normal gravity, can take place during the transients. In the present paper we will consider a cylinder with uniform volumetric heating and an isothermal outer boundary. Steady state flows for this problem represent pseudosteady-state solutions (Lin & Akins 1986; Hutchins & Marschall 1989) of the transient food-processing problem when, in the latter, the wall temperature is spatially uniform and all temperatures increase or decrease linearly with time.

† Present address: Mechanical Engineering, State University of New York at Stony Brook, Stony Brook, NY 11794, USA.
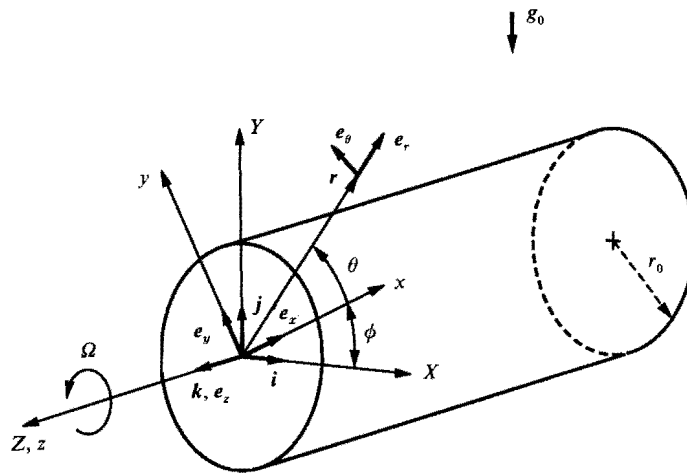
FIGURE 1. Schematic of cylindrical geometry and coordinates. The cylinder rotates at angular velocity Ω. The inertial coordinates are (X, Y, Z) and the rotating coordinates are (x, y, z) and (r, θ, z).

Most studies of convection in horizontal non-rotating cylinders have focused on the effects of spatially-non-uniform wall heating (Ostrach 1972). Spatially-uniform wall heating (flux or temperature) leads to inherently transient flows in the absence of a heat sink. Only the studies by Van Sant (1969) and Takeuchi & Cheng (1976) with internal heating and a cooled outer boundary closely match the thermal conditions of the present study. Van Sant carried out experiments to study vertical centreline temperatures, whereas Takeuchi & Cheng carried out transient numerical calculations of pseudosteady-state convection.

For combined rotation and natural convection in horizontal cylinders relatively few geometries have been studied. One system involves the orbital rotation of a heated pipe (with a throughflow of coolant) about an offset parallel axis (Woods & Morris 1980; Mori & Nakayama 1967). However, the effect of the rotation of the pipe about its own axis, and the effect of the external normal-gravity field, were small or were neglected. A geometry more closely related to the present study is that of Yang *et al.* (1988), who considered natural convection in a rotating, horizontal cylinder with an applied axial temperature gradient. Steady three-dimensional flows were obtained numerically allowing for both axial rotation and normal gravity. Rotation was observed to inhibit natural convection and endwall heat transfer. By contrast, flows driven by radial temperature gradients are of interest in the present study.

The effects of rotation and natural convection have been examined in cylindrical annuli with differentially heated walls, in horizontal (Fusegi, Farouk & Ball 1986; Lee 1984) and vertical (Randriamampianina, Bontoux & Roux 1987; Busse 1986) arrangements. The studies by Hide (1967) and Hide & Mason (1970, 1974) appear to be the most relevant. They examined gravitationally-driven motions in statically stable fluids in a vertical annulus. The annulus rotated rapidly so that gyroscopic torques inhibited overturning in meridianal planes. This led to non-axisymmetric flows (baroclinic waves) sometimes called sloping convection. Some of the flows at high rotational rates in an internally-heated annulus with vanishing inner-cylinder radius resemble those of the present study.

The geometry considered in the present paper is sketched in figure 1. A long, fluid-filled, horizontal cylinder in a vertical gravity field, g_0, is subjected to a steady

angular velocity, Ω, about its axis. We assume a uniform volumetric heat generation in the cylinder and an isothermal outer boundary at $r = r_0$, and seek transient and steady two-dimensional solutions in the (r, θ)-plane. With internal heating, to keep the appropriate sign for the radial body force, the latter is attributed to self-gravitation in the cylinder. However, the resulting flows are exactly the same as if we had assumed uniform internal cooling and a radial body force due to centrifugal acceleration. It will be convenient in the following to formulate the problem with an emphasis on uniform heating and self-gravitation.

2. Mathematical formulation

2.1. *Governing equations*

The coordinates are shown in figure 1. The coordinate system (X, Y, Z) with unit vectors (i, j, k) is in an inertial frame, while the coordinate system (x, y, z) with unit vectors (e_x, e_y, e_z) rotates counterclockwise with the cylinder at a constant angular velocity Ωk. The polar coordinate system (r, θ, z) with unit vectors (e_r, e_θ, e_z) will also be used and is in the rotating frame. The angle between the inertial and rotating frames is denoted by ϕ.

Reference quantities used for non-dimensionalization are as follows: for length, the cylinder radius, r_0; for time, r_0^2/α; for temperature difference, $\dot{Q}'''r_0^2/k$; and for pressure, $\rho_0 \alpha^2/r_0^2$; where $\dot{Q}'''$ is the uniform volumetric rate of heat generation in the cylinder and α, k and ρ_0 are the thermal diffusivity, thermal conductivity, and reference density, respectively, of the fluid.

The non-dimensional Boussinesq equations for motion in the rotating coordinate frame, driven by normal gravity and a radial force field, are

$$\nabla \cdot u = 0, \tag{1}$$

$$\frac{\partial u}{\partial t} + u \cdot \nabla u + Re\,Pr\,k \times u = -\nabla p + Pr\,\nabla \cdot (\nabla u + (\nabla u)^*) + Ra_r\,Pr\,Tx + Ra_g\,Pr\,TB(t), \tag{2}$$

$$\frac{\partial T}{\partial t} + u \cdot \nabla T = \nabla^2 T + H, \tag{3}$$

where $u = (u, v, w)$ is the velocity vector in the (x, y, z) rotating frame, t is time, p is the reduced pressure (i.e. pressure due wholly to fluid motion), T is temperature, and $x = (x, y, 0)$ is the radial position vector. Temperature is defined by $T = (T' - T_0')/(\dot{Q}'''r_0^2/k)$, where a single prime denotes dimensional temperature and T_0' is the uniform, constant temperature of the outer boundary of the cylinder. The asterisk in the viscous term of (2) denotes a transpose. In the energy equation (3), H represents volumetric heating and is of unit magnitude.

In the momentum equation (2), the third term on the left-hand side is the Coriolis term. On the right-hand side, the third and fourth terms arise from buoyancy forces due to radial gravity and normal gravity, respectively. The momentum equation introduces four parameters:

$$Ra_r = \frac{g'\beta(\dot{Q}'''r_0^2/k)\,r_0^3}{\nu\alpha}, \quad Ra_g = \frac{g_0\beta(\dot{Q}'''r_0^2/k)\,r_0^3}{\nu\alpha}, \quad Re = \frac{2\Omega r_0^2}{\nu}, \quad Pr = \frac{\nu}{\alpha}, \tag{4}$$

which are, respectively, the radial-gravity Rayleigh number, the normal-gravity Rayleigh number, the rotational Reynolds number, and the Prandtl number. Appearing therein are the kinematic viscosity, ν, the volume expansion coefficient,

β, the radial acceleration of gravity g', and the vertical acceleration of gravity in the inertial frame, g_0.

The radial gravity in a self-gravitating cylinder is given by $g' = 2\pi\rho_0 Gr_0$, where G is the universal gravitational constant. When rotational effects cause the radial acceleration, $g' = -\Omega^2 r_0$. However, if we also change the sign of $\dot{Q}'''$, Ra_r remains positive. Thus, radial buoyancy effects in a centrifugally-driven, internally-cooled cylinder are similar to those in a self-gravitating, internally-heated cylinder. With this in mind, when centrifugal forces are important we can take $g' = |-\Omega^2 r_0| = \Omega^2 r_0$.

The normal gravity, g_0, is fixed in the inertial frame; its apparent rotation in the rotating frame is expressed by $\boldsymbol{B}(t)$ in (2), where

$$\boldsymbol{B}(t) = (\sin\tfrac{1}{2}Re\,Pr\,t, \cos\tfrac{1}{2}Re\,Pr\,t, 0) \tag{5a}$$

$$= (\sin(\tfrac{1}{2}Re\,Pr\,t+\theta), \cos(\tfrac{1}{2}Re\,Pr\,t+\theta), 0) \tag{5b}$$

in (x, y, z) and (r, θ, z) coordinates, respectively. For reference, one non-dimensional period of rotation of the normal gravity vector is given by

$$P = \frac{4\pi}{Re\,Pr}. \tag{6}$$

The present problem is governed by the four non-dimensional groups Ra_r, Ra_g, Re, and Pr defined in (4). We will regard these as independent. The exception is in §5.4 when centrifugal forces are considered. There, Re is replaced by another parameter so that Ω appears only in Ra_r. To complete the problem formulation, the initial state of the fluid is assumed to be isothermal, rigid-body rotation with $\boldsymbol{u} = p = T = H = 0$. Heating is presumed to start for $t > 0$, with $H = 1$ inside the cylinder and $\boldsymbol{u} = T = 0$ at the outer boundary of the cylinder.

2.2. *Secondary variables* (ψ, ζ, Nu)

For diagnostic purposes it is convenient to introduce the stream function, ψ, and the z-component of vorticity, ζ, in a rotating frame:

$$u_r = \frac{1}{r}\frac{\partial\psi}{\partial\theta}, \quad u_\theta = -\frac{\partial\psi}{\partial r},$$

$$\zeta = -\left(\frac{1}{r}\frac{\partial}{\partial r}\left(r\frac{\partial}{\partial r}\right) + \frac{1}{r^2}\frac{\partial^2}{\partial\theta^2}\right)\psi. \tag{7}$$

Furthermore, the local Nusselt number at the surface of the cylinder is given by

$$Nu = -2(\boldsymbol{\nabla}T + \boldsymbol{u}T)\cdot\boldsymbol{n}, \tag{8}$$

where $\boldsymbol{n}$ is the outward normal. The total heat generated within the cylinder is

$$\int_0^{2\pi}\int_0^1 Hr\,\mathrm{d}r\,\mathrm{d}\theta = \pi, \tag{9}$$

where $H = 1$ is assumed. At steady state, the generated heat escapes across the outer surface of the cylinder with an average Nusselt number of $+1$, a result which is independent of the strength of fluid motion. The local value of Nu, however, typically varies over the outer surface of the cylinder.

2.3. *Two-dimensionality*

A two-dimensional motion is the (r, θ)-coordinates of the cylinder is considered; thus the Coriolis force has no dynamic significance. It could actually be absorbed in the

pressure term if the pressure is redefined as p-ψ (Greenspan 1969), but this has not been done for reasons discussed in Ladeinde (1988) related to numerical error control. Rotation thus contributes to the dynamics of the flow only through the centrifugal buoyancy term in (2) and the appearance of Re in the phase angle associated with the apparent rotation of the normal gravity. Because of the foregoing, the similarity between flows in the present study and some of those in studies of baroclinic waves cannot be explained in terms of gyroscopic torques, but rather in terms of the baroclinicity of the two systems (defined here as the vorticity production by density gradients).

3. Stability of the basic state

We here consider the stability of an internally-heated cylinder subjected to radial gravity. The basic state in an internally-heated cylinder is

$$T_e = \tfrac{1}{4}(1 - r^2), \quad u_r = u_\theta = 0, \tag{10}$$

where T_e is the rest state temperature. The associated Nusselt number at the surface of the cylinder is $Nu = 1$.

For the present problem, the Euler–Lagrange equations that result from the variational problem

$$\Upsilon_\epsilon = \underset{(\tilde{u}, \tilde{T}) \in \Upsilon}{\text{maximum}} \frac{-(1 + \tfrac{1}{2}\lambda) \langle r\tilde{u}_r \tilde{T} \rangle}{\langle \boldsymbol{\nabla} \tilde{u} : \boldsymbol{\nabla} \tilde{u} \rangle + \lambda \langle \boldsymbol{\nabla} \tilde{T} \cdot \boldsymbol{\nabla} \tilde{T} \rangle} \tag{11}$$

are the same as the equations that govern the linearized perturbations of the basic state. In the foregoing expression, Υ is a linear vector space of couples $(\tilde{u}, \tilde{T})$, containing a solenoidal perturbation velocity vector field and an associated perturbation scalar temperature field which satisfy $\tilde{u} = \tilde{T} = 0$ on the walls of the cylinder. The angular brackets denote integration over the domain and λ is a coupling parameter often used in energy stability analyses of the Boussinesq equations (Joseph 1966). λ has a maximum value of two for the present problem. Energy and linear stability results thus coincide, preventing a subcritical bifurcation. Further, the linear equations are self-adjoint (Ladeinde 1988), and an oscillatory instability cannot occur when fluid motion starts. This is the principle of exchange of stability, which follows because the cylinder wall in our system is cooled when the radial gravity force is directed toward the centre but heated when the radial gravity is directed outward. A direct release of potential energy is not possible otherwise, and flow sets in in an oscillatory fashion.

With the foregoing, the equation governing the non-axisymmetric perturbation stream function ψ is

$$\left(D^* D - \frac{n^2}{r^2} \right)^3 \psi_0 = -\tfrac{1}{2} Ra_r n^2 \psi_0, \tag{12}$$

where
$$D \equiv \frac{d}{dr}, \quad D^* \equiv \left(\frac{1}{r} + \frac{d}{dr} \right),$$

n is the azimuthal wavenumber, and

$$\psi = \psi_0(r) e^{in\theta}. \tag{13}$$

n	$Ra_{r,c}$
1	13738
2	16577
3	24284
4	35928
5	52016
6	73298

TABLE 1. Values of $Ra_{r,c}$ at the onset of convection in an internally-heated, self-gravitating cylinder as a function of azimuthal wavenumber, n

The boundary conditions are:

$$r = 0: \quad \frac{\partial \psi_0}{\partial r} = \text{finite}, \quad \psi_0 = 0.$$

$$r = 1: \quad \psi_0 = \frac{\partial \psi_0}{\partial r} = \left(\text{D*D} - \frac{n^2}{r^2} \right)^2 \psi_0 = 0.$$

The linear combination

$$\psi_0 = \sum_{k=1}^{3} C_k J_n (\lambda_\kappa^{\frac{1}{2}} r)$$

(where C_3 is the complex conjugate of C_1 and J_n is a Bessel function of the first kind) is a general solution of (12) (Joseph & Carmi 1969) provided that

$$\lambda_1 = A^{\frac{1}{3}} \exp(0), \quad \lambda_2 = A^{\frac{1}{3}} \exp(-\tfrac{2}{3}\pi i), \quad \lambda_3 = A^{\frac{1}{3}} \exp(\tfrac{2}{3}\pi i),$$

where

$$A \equiv \tfrac{1}{2} Ra_r n^2.$$

Application of the boundary conditions and the requirement of a non-vanishing solution gives the critical values of Ra_r at the onset of convection. These values are denoted by $Ra_{r,c}$ and are listed in table 1. The minimum value is $Ra_{r,c} = 13738$, corresponding to a two-cell flow and $n = 1$.

4. Numerical method for finite-amplitude flows

Large-amplitude flows in the (r, θ)-plane have been obtained numerically with a Galerkin finite-element method. A consistent penalty formulation with time integration error control has been used (Gresho, Lee & Sani 1980).

The appropriate expansions in finite-dimensional, piecewise-polynomial basis sets, with all boundary conditions formally treated as natural, are:

$$u = U^*(t)\, \xi_1(x), \tag{14}$$

$$p = D^*(t)\, \xi_2(x), \tag{15}$$

$$T = \Theta^*(t)\, \xi_1(x), \tag{16}$$

and

$$x = L^*\xi_3(x). \tag{17}$$

On an element basis, U, D, Θ and L are vectors containing the values of the variables u, p, T and x at appropriate nodes, where x is the position vector, and ξ_1, ξ_2 and ξ_3 are vectors of interpolation functions. Asterisks denote a transpose.

The system of nonlinear ordinary differential equations obtained by applying the Galerkin finite element method to (1)–(3) is

$$\boldsymbol{C}^*U = 0 \tag{18}$$

$$\boldsymbol{M}_1\dot{U} + \boldsymbol{S}_1(U)U - \boldsymbol{C}D + \boldsymbol{H}\boldsymbol{\Theta} = \boldsymbol{F}_1(\boldsymbol{\Theta}), \tag{19}$$

$$\boldsymbol{M}_2\dot{\boldsymbol{\Theta}} + \boldsymbol{S}_2(U)\boldsymbol{\Theta} = \boldsymbol{F}_2. \tag{20}$$

The matrix $\boldsymbol{S}_1$ contains the contributions from the nonlinear convective terms of the momentum equation, the Coriolis term, and the viscous diffusion terms, while $\boldsymbol{H}$ contains the buoyancy terms. Matrix $\boldsymbol{S}_2$ contains the nonlinear convective terms and the thermal diffusion terms of the energy equation. $\boldsymbol{F}_1$ and $\boldsymbol{F}_2$ result from the natural boundary conditions of the problem and the volumetric heat source. $\boldsymbol{C}$ is the divergence matrix associated with a pressure-weighted continuity equation, and $\boldsymbol{M}_1$ and $\boldsymbol{M}_2$ are the mass and heat capacity matrices, respectively. Equations (18)–(20) can be combined and written as:

$$\boldsymbol{M}\dot{v} + \boldsymbol{G}v = f, \tag{21}$$

where $\qquad\qquad\qquad v = (U, D, \boldsymbol{\Theta}).$

For the spatial integrations embedded in $\boldsymbol{M}$, $\boldsymbol{G}$ and f of (21), we have used nine-node Lagrange quadrilateral elements with biquadratic interpolation for $\boldsymbol{u}$ and T, and a three-node discontinuous interpolation for p. The eight-node serendipity element has been used to map the geometry $\boldsymbol{x}$ of the nine-node element. Depending on flow parameters, the spatial mesh used for the computations consisted of 201–649 grid points, with appropriate local refinements when needed to resolve boundary layers.

For the time integration of (21), temporal truncation error estimates are used to vary the timestep size so that a given level of time integration accuracy is assured even if the timesteps become large. Timestep sizes are determined by the temporal physics of the flow (Gresho *et al.* 1980). (The present scheme should not be confused with explicit time integration schemes in which timesteps are adaptively calculated to satisfy numerical stability requirements.) The error control scheme used predictor and corrector steps to march over a timestep; these steps respectively employ Adams–Bashforth and trapezoid rule formulae. The Newton–Raphson procedure is used to linearize the nonlinear algebraic equations obtained from the time and space integrations of (21).

The foregoing time integration scheme is appropriate for the present problem since it allows all timescales of motion that occur during one revolution to be resolved to an acceptable overall level of accuracy. This is important, since the timescales of interest (i.e. for warm-up) may be orders of magnitude larger than a period of rotation.

The code has been subjected to many tests to establish its validity. The tests include standard diffusion and convection problems (e.g. Vahl Davis 1983), critical wavenumber and flow stability calculations, and finite-amplitude flows in a cylinder. An example of the latter is shown in figure 2, where numerical solutions are compared with experimental data from Sabzevari & Ostrach (1974). The experiments employed a non-rotating horizontal cylinder subjected to a wall temperature $T = \cos\theta$ while in a vertical gravity field. Other parameters were $Ra_g = 4.464 \times 10^4$ and $Pr = 1.86 \times 10^4$. Steady-state temperature and velocity profiles, respectively, are shown in figure 2(*a,b*) for the horizontal ($\theta = 0$) and vertical ($\theta = \frac{1}{2}\pi$) diameters. Close agreement is apparent.
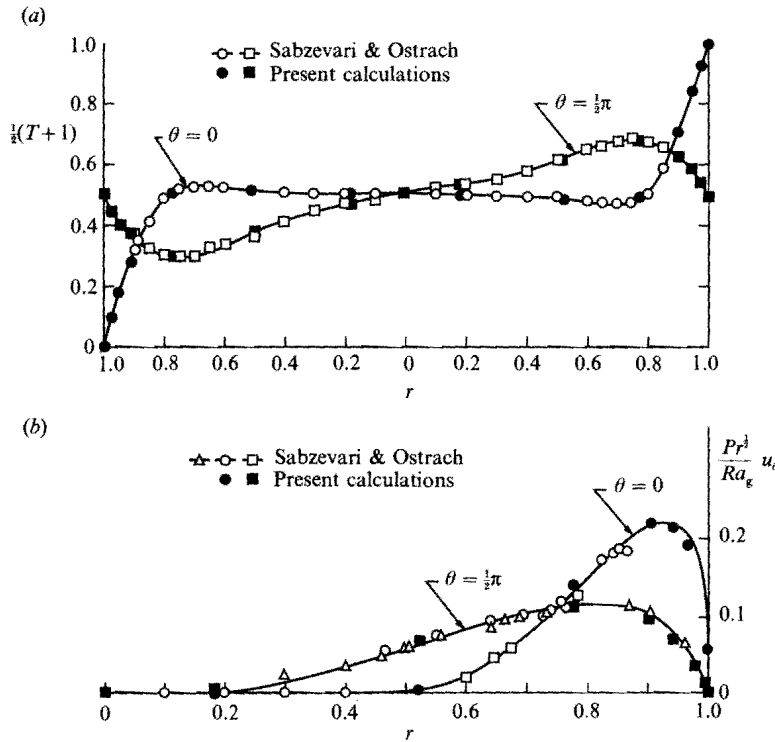
(a)

(b)

FIGURE 2. Comparison of numerical results with the experimental data of Sabzevari & Ostrach (1974). Steady state profiles are shown along the horizontal ($\theta = 0$) and vertical ($\theta = \frac{1}{2}\pi$) diameters. (a) Temperature, T. (b) Velocity, u_θ.

Further details on the implementation of the method, as well as the numerical procedures used for the secondary variables (ζ, ψ, Nu), are available in Ladeinde (1988).

5. Finite-amplitude flows

Time-dependent, finite-amplitude convective flows in an internally-heated horizontal cylinder are discussed in the following sections for four cases: radial gravity dominant ($0 \leqslant Ra_r \leqslant 10^6$, $Ra_g = Re = 0$); normal gravity dominant ($0 \leqslant Ra_g \leqslant 10^6$, $Ra_r = Re = 0$); combined normal gravity and rotation ($Ra_g = 10^5$, $0 \leqslant Re \leqslant 250$, $Ra_r = 0$); and combined radial gravity, normal gravity, and rotation ($Ra_r = 10^5$, $10^3 \leqslant Ra_g \leqslant 10^6$, $0 \leqslant Re \leqslant 250$). Solutions were obtained numerically. In all cases, the Prandtl number was fixed at $Pr = 7.0$.

5.1. Radial gravity dominant

In this section we consider steady and transient convective motions driven by radial gravity at supercritical values of Ra_r. The effects of normal gravity and cylinder rotation are neglected ($Ra_g = Re = 0$). With radial gravity dominant, and when due to self-gravitation, positively and negatively buoyant fluid parcels experience, respectively, radially-outward and radially-inward body forces.
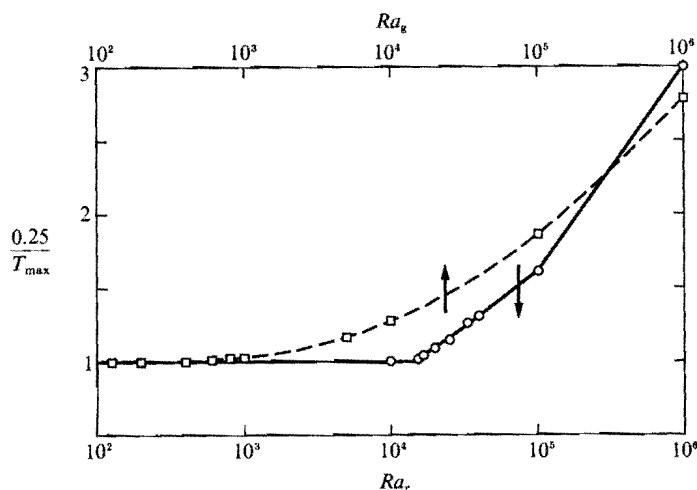
FIGURE 3. Temperature ratio $0.25/T_{max}$ for radial gravity convection (——) and normal gravity convection (– – –).

5.1.1. *Steady states*

In general, the fluid is more vigorously mixed with increasing Ra_r, leading to a lower maximum temperature in the interior. The behaviour of the steady-state heat transport with increasing Ra_r is shown by the solid line in figure 3. The ordinate is $0.25/T_{max}$, where 0.25 represents the maximum interior temperature associated with the conduction solution and T_{max} is the maximum steady-state interior temperature at any Ra_r. The critical Rayleigh number at the onset of convection, $Ra_{r,c}$, as inferred from figure 3, is within 2% of the theoretical value obtained in §3. Consistent with linear theory, a two-cell flow is observed at the onset of motion. The ordinate in figure 3 increases almost linearly in the region of two-cell flows ($Ra_{rc} \leqslant Ra_r \leqslant 10^5$), and more rapidly thereafter in a four-cell flow region.

Steady-state flow and temperature fields are shown in figure 4 (*a–d*) for four values of Ra_r: $Ra_r = 1.66 \times 10^4, 2.5 \times 10^4, 10^5$, and 10^6. As noted earlier, the two-cell flow predicted by linear theory persists until $Ra_r = 10^5$, although the augmentation of heat transfer by fluid motion is apparent at the higher Ra_r values. The four-cell pattern at $Ra_r = 10^6$ consists of a pair of small, weakly-circulating cells and a second pair of larger, stronger cells. This convection pattern is efficient at transporting heat so that a substantial portion of the interior is essentially isothermal. Vorticity and pressure gradients are important at the larger Ra_r values, and are found in the wall regions where $\partial T/\partial \theta$ is large. These are also the regions with low heat flux, where thermal boundary layers 'peel off' from the wall of the cylinder.

One remarkable difference between the large-amplitude flows driven by radial gravity and those driven by normal gravity (to be discussed in §5.2) is the absence of a relatively stagnant, thermally-stratified interior in radial gravity flows. Indeed, the strength of the interior flow is comparable to that in the wall boundary layers. This leads to effective heat transport and to a more uniform temperature in the interior. Note also that the orientation of the cells (and hence the locations of high and low heat fluxes) cannot be predicted in advance for radial gravity flows. This is analogous to the so-called horizontal isotropy of the Rayleigh–Bénard problem. The initial condition or the solution at short time probably determines the orientation of the steady-state pattern (Ladeinde & Torrance 1990).
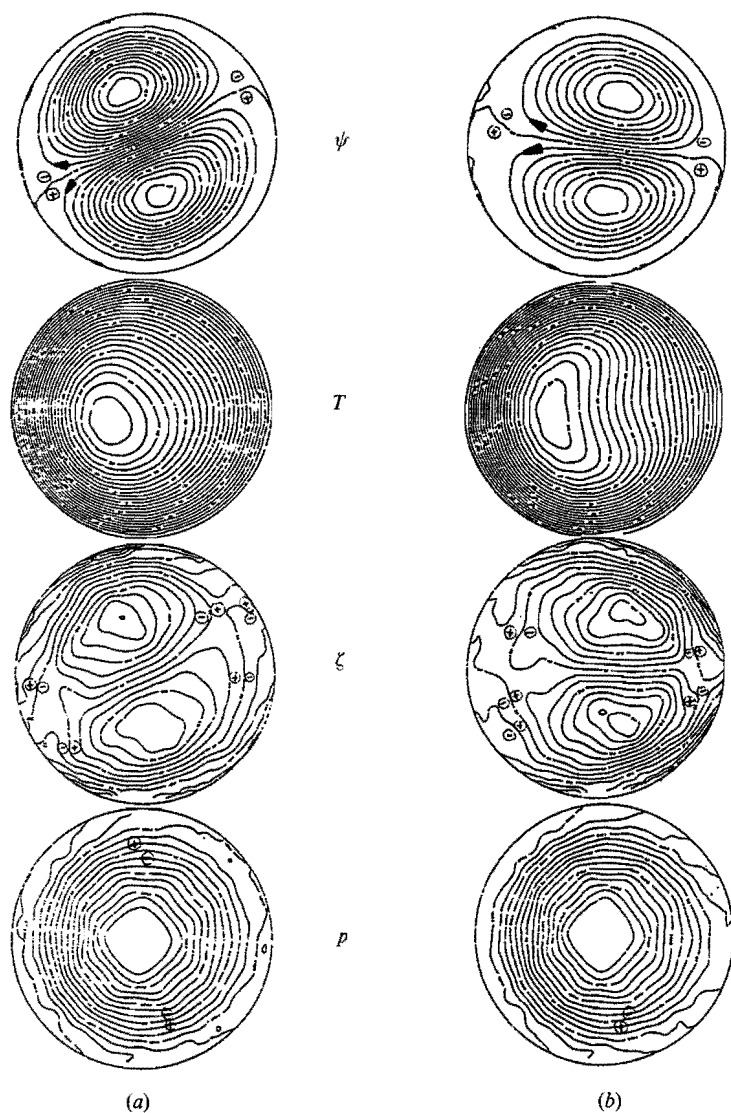
(a)   (b)

FIGURE 4 (a,b). For caption see facing page.

5.1.2. *Transients*

With the onset of internal heating, the temporal development of radial gravity flows from rest displays a novel and complex behaviour. The transient for $Ra_r = 10^5$ is shown in figure 5, and is representative of results observed at all Ra_r values studied. Although a coarse grid was used for the figure, grid refinement does not affect the qualitative picture.

In figure 5, high-wavenumber modes are excited immediately after the start of heating, and a convection pattern that looks like sixteen cells (azimuthal wavenumber $n = 8$) is observed at $t = 0.0039$. At early times, convection is restricted to a thin circumferential layer at the wall so that a high-wavenumber pattern results. However, because the disturbances at short times are weak (temperature is

FIGURE 4. Steady-s
p, for radial-gravity
$\psi = -1.3\,(0.1)\,1.3;\ T$
$-2.4\,(0.3)\,2.7;\quad T =$
$-5.6\,(0.8)\,6.4;\quad T =$
$\psi = -14\,(2)\,22;\quad T =$

essentially condu
according to line
mode by $t = 0$.
subsequent evolv
a two-cell mode
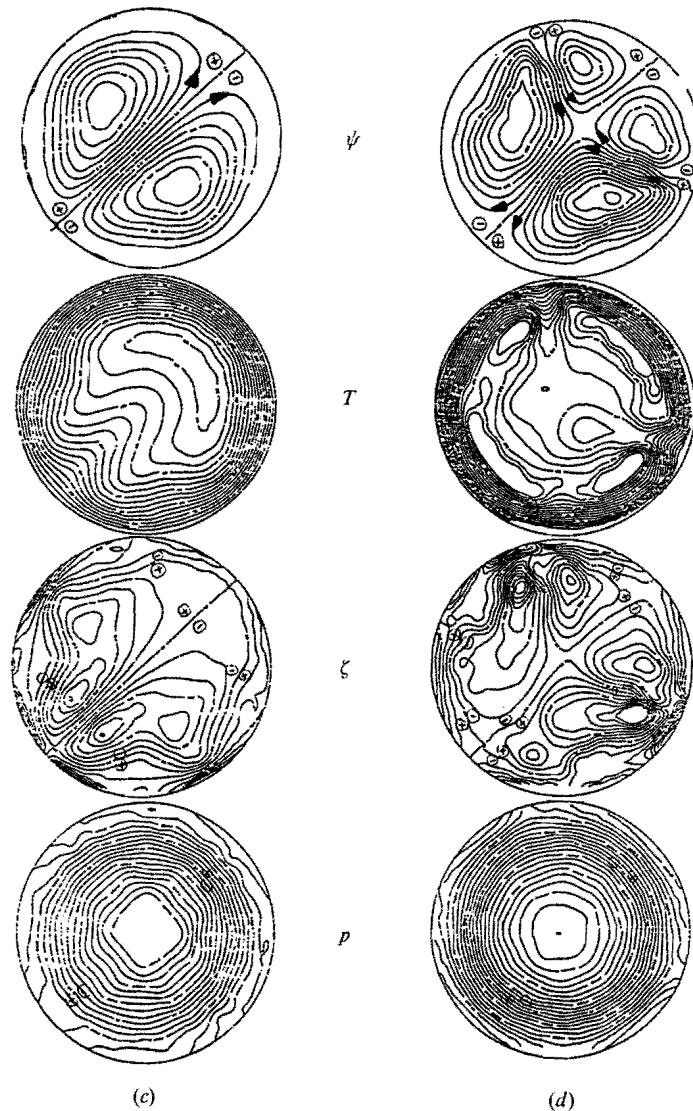$Ra_r < 10^5$. At Rc
conduction temp
cell pattern, onc

(c) (d)

FIGURE 4. Steady-state contours of stream function, ψ, temperature, T, vorticity, ζ, and pressure, p, for radial-gravity driven convection at four values of Ra_r with $Ra_g = Re = 0$. (a) $Ra_r = 1.66 \times 10^4$: $\psi = -1.3\,(0.1)\,1.3$; $T = 0\,(0.01)\,0.24$; $\zeta = -30\,(5)\,40$; $p = -4000\,(500)\,3500$. (b) $Ra_r = 2.5 \times 10^4$: $\psi = -2.4\,(0.3)\,2.7$; $T = 0\,(0.01)\,0.22$; $\zeta = -63\,(9)\,72$; $p = -5600\,(700)\,5600$. (c) $Ra_r = 1 \times 10^5$: $\psi = -5.6\,(0.8)\,6.4$; $T = 0\,(0.01)\,0.16$; $\zeta = -210\,(30)\,240$; $p = -18\,000\,(2000)\,18\,000$. (d) $Ra_r = 1 \times 10^6$: $\psi = -14\,(2)\,22$; $T = 0\,(0.005)\,0.085$; $\zeta = -800\,(100)\,700$; $p = -11 \times 10^4\,(10^4)\,11 \times 10^4$.

essentially conduction), the lower-wavenumber modes have a growth rate advantage according to linear theory. Thus, the sixteen-cell mode is replaced by an eight-cell mode by $t = 0.067$. The strength of convection is still weak, promoting the subsequent evolution of a four-cell pattern. This cascade process eventually produces a two-cell mode at steady state. Thus, the linear theory is quite important for $Ra_r < 10^5$. At $Ra_r = 10^6$, the initial flows are stronger than those in figure 5, and the conduction temperature profile is modified earlier in the transient. Further, a four-cell pattern, once formed, gets locked-in and dominates the steady state.
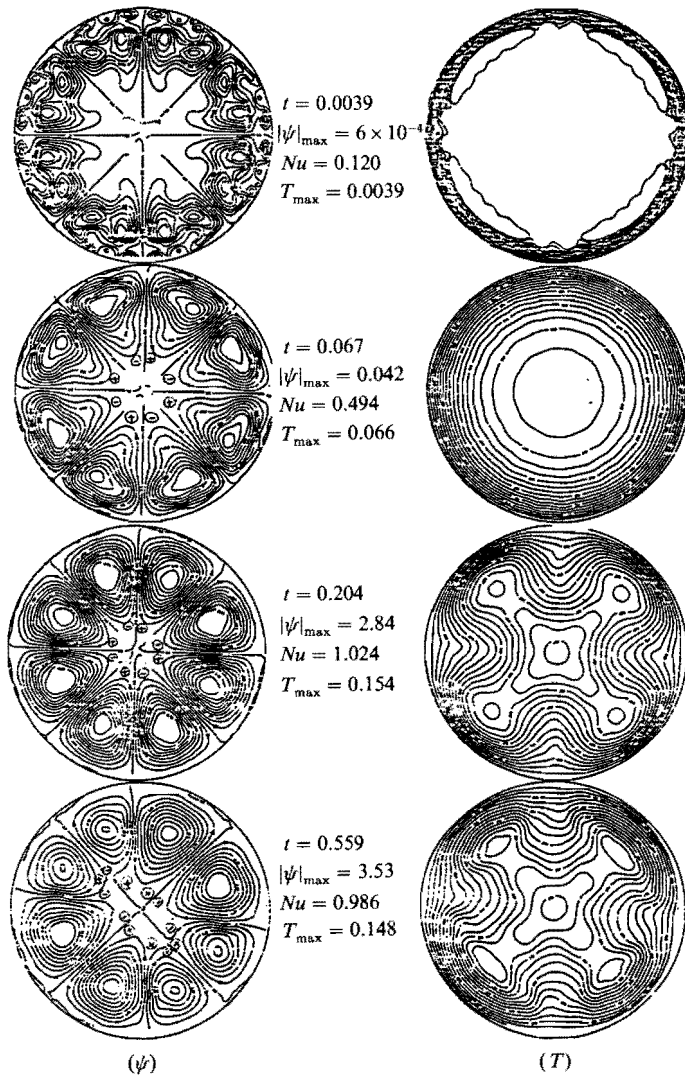
$t = 0.0039$
$|\psi|_{max} = 6 \times 10^{-4}$
$Nu = 0.120$
$T_{max} = 0.0039$

$t = 0.067$
$|\psi|_{max} = 0.042$
$Nu = 0.494$
$T_{max} = 0.066$

$t = 0.204$
$|\psi|_{max} = 2.84$
$Nu = 1.024$
$T_{max} = 0.154$

$t = 0.559$
$|\psi|_{max} = 3.53$
$Nu = 0.986$
$T_{max} = 0.148$

(ψ) (T)

FIGURE 5. For caption see facing page.

FIGURE 5. Transien

The transient cell-size adjustments observed in the present cylindrical geometry are qualitatively similar to those observed in horizontal layers heated from below (Chen & Whitehead 1968; Daniels 1984; Gollub, McCarrier & Steinman 1982). During transients from rest in horizontal layers, initial high-wavenumber motions are observed to evolve in time to lower-wavenumber forms with cell aspect ratios close to unity.

5.2. *Normal gravity dominant*

When normal gravity is dominant, the convective flow structure is determined by the orientation of the gravity vector in the inertial reference frame. Steady and transient convective flows for $0 \leqslant Ra_g \leqslant 10^6$ are summarized in this section. The effects of radial gravity and rotation are neglected ($Ra_r = Re = 0$).

The general beha
shown by the dashe
temperatures do not
Above this value,
smoothly with incre

The preferred mo
in figure 6(a) for Ra_g
with upflow on the
Cheng (1976). Resul
later sections.

Horizontal and v

$t = 0.617$
$|\psi|_{max} = 6.20$
$Nu = 1.010$
$T_{max} = 0.140$

$t = 1.452$
$|\psi|_{max} = 6.04$
$Nu = 0.946$
$T_{max} = 0.141$

$t = 1.515$
$|\psi|_{max} = 7.71$
$Nu = 0.942$
$T_{max} = 0.148$

$t = 1.607$
$|\psi|_{max} = 6.06$
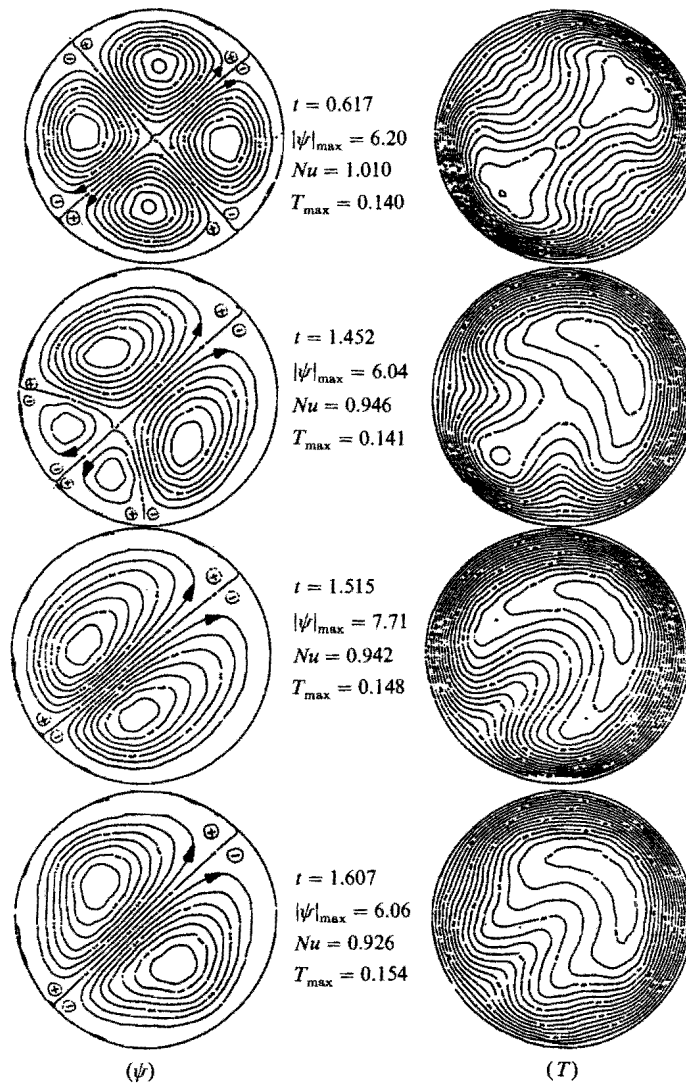$Nu = 0.926$
$T_{max} = 0.154$

(ψ) (T)

FIGURE 5. Transient evolution from a rest state showing mode switching in radial-gravity driven convection. $Ra_r = 10^5$, $Ra_g = Re = 0$.

The general behaviour of the steady-state heat transport with increasing Ra_g is shown by the dashed line in figure 3. Although fluid motion occurs for all $Ra_g > 0$, temperatures do not depart significantly from the conduction field until $Ra_g > 400$. Above this value, the maximum temperature in the interior, T_{max}, decreases smoothly with increasing Ra_g.

The preferred motion for all Ra_g values studied consists of two cells, as sketched in figure 6(a) for $Ra_g = 10^5$. The two cells are aligned with the external gravity vector with upflow on the vertical diameter. The flow structure agrees with Takeuchi & Cheng (1976). Results in figure 6 are included, however, to help interpret results in later sections.

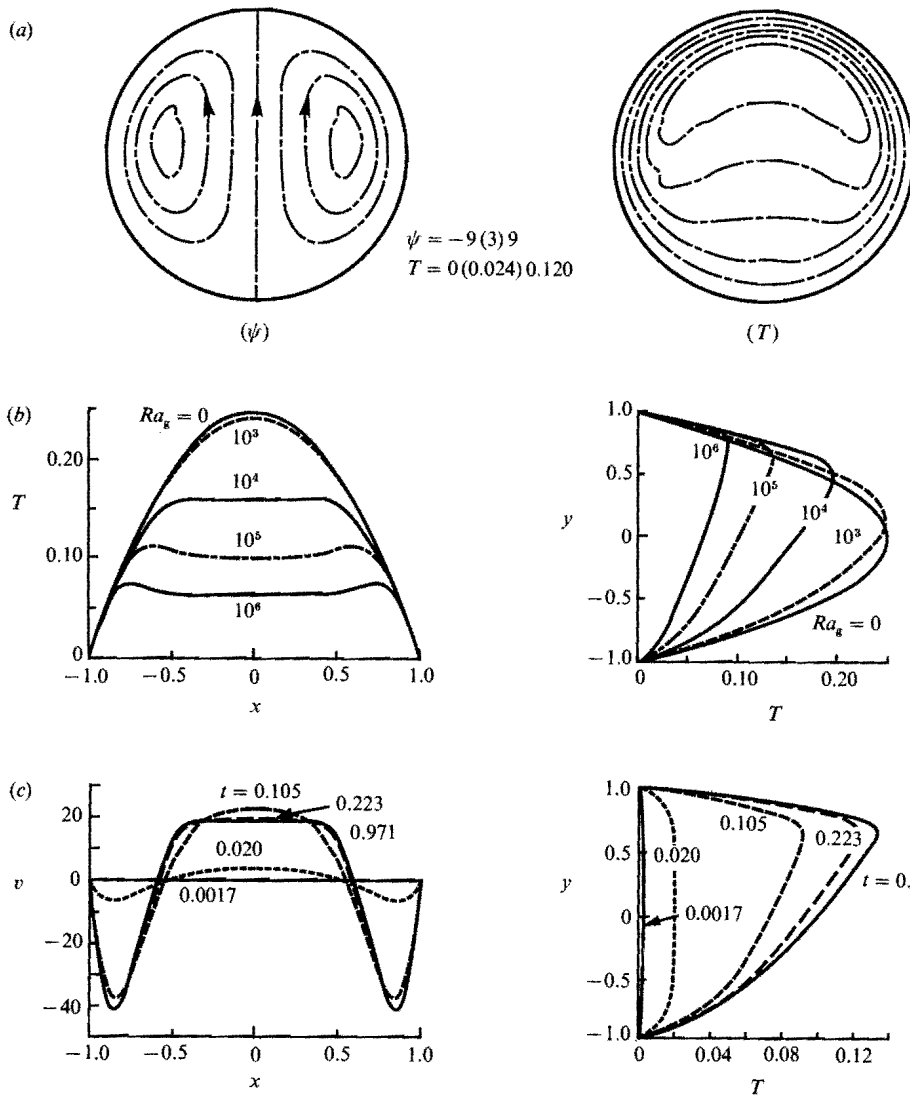Horizontal and vertical temperature profiles are shown in figure 6(b) for a range

FIGURE 6. Normal-gravity driven convection. $Ra_r = Re = 0$. (a) Steady state streamlines and isotherms for $Ra_g = 10^5$. (b) Steady-state temperature profiles along the horizontal (x) and vertical (y) diameters for various values of Ra_g. (c) Transient profiles of vertical velocity, v, along the horizontal diameter and temperature, T, along the vertical diameter for $Ra_g = 10^5$.

of Ra_g values. When $Ra_g < 10^4$ the internally-generated heat is transported mainly by molecular diffusion, although the effect of fluid motion is manifested at $Ra_g = 10^3$ in the movement of the hottest region away from the centre of the cylinder. The convective transport of heat becomes important at higher Ra_g values. At $Ra_g = 10^5$ and 10^6, convection of heat by the vertical component of velocity (i.e. $v\partial T/\partial y$) is the major transport term in the interior. Note however, that $u \ll 1$ (except where the fluid turns at $\theta = \pm\frac{1}{2}\pi$), $\partial T/\partial x$ is very small in the interior, and the interior is thermally stratified in the vertical. The foregoing suggests that molecular diffusion is negligible in the interior. Thus, the steady energy balance in the interior is between the internal heat generation, H, and $v\partial T/\partial y$. In the wall region, the balance is
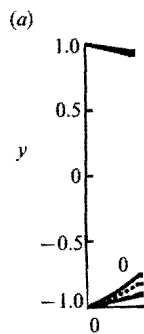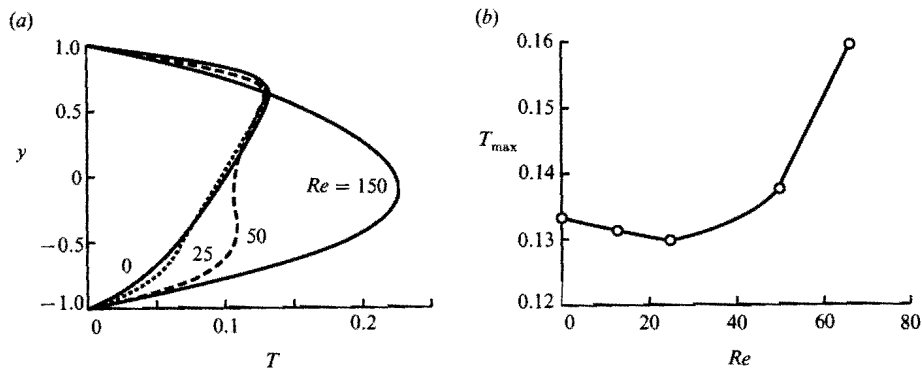
FIGURE 7. Combined rotation and normal-gravity driven convection. Re varied with $Ra_g = 10^5$ and $Ra_r = 0$. (a) Steady-state temperature profiles along the vertical diameter. Results shown at $\phi = 0$ (normal gravity vector aligned with y-coordinate). (b) T_{max} vs. Re.

between H and $\nabla^2 T$, while in the transition region between the wall and the interior the internally-generated heat is transported by diffusion and convection.

The transients with normal gravity are rather simple, as compared to those with radial gravity. Representative transient velocity and temperature profiles are shown in figure 6(c) for $Ra_g = 10^5$. A two-cell flow, with thermal stratification in the interior, develops with time. For all Ra_g values, the bicellular pattern appeared immediately after heat input and was maintained throughout the transients without any mode changes.

5.3. *Combined normal gravity and rotation*

In this section the effects of rotation on convection driven by normal gravity are examined. Radial gravity is neglected. The rotational effects formally arise from the terms containing Re in (2) and (5). Parameter values considered are $Ra_g = 10^5$, $0 \leqslant Re \leqslant 250$, and $Ra_r = 0$. Studies were also carried out for $Ra_g = 10^4$ but qualitatively similar results were obtained.

For $0 \leqslant Re \leqslant 50$, the two identical cells produced in the inertial frame by normal gravity tend to coalesce into a single cell pattern that steadily revolves in a clockwise sense around an observer in the rotating frame. The observer sees a main cell that occupies most of the cylinder and a smaller, slowly-rotating secondary cell in a 'corner' of the cylinder. The secondary cell diminishes in size (strength) with increasing Re and disappears at about $Re = 50$. The flow patterns for larger Re values are inefficient at transporting heat (figure 7a). The flow strength as well as the efficiency of heat transport, as inferred from T_{max}, reach a maximum at $Re \approx 25$ and decrease on either side of this value (figure 7b). The flow is very weak at the largest Re values studied, and appears as a rigid-body rotation when observed in the inertial frame. Heat transport is essentially by molecular diffusion.

The time-dependent behaviour is illustrated in figure 8 for the case $Ra_g = 10^5$, $Re = 25$. The pattern observed in the rotating frame at short time is the same two-cell pattern observed in the inertial frame, with the cells aligned with the instantaneous direction of the normal gravity vector (shown by large arrows) which rotates clockwise. The shapes of the cells are distorted during the transient as the steadily rotating pattern evolves, with one cell growing at the expense of the other. The flow achieves a true steady state when viewed in the inertial frame, and a periodic steady state when viewed in the rotating frame.
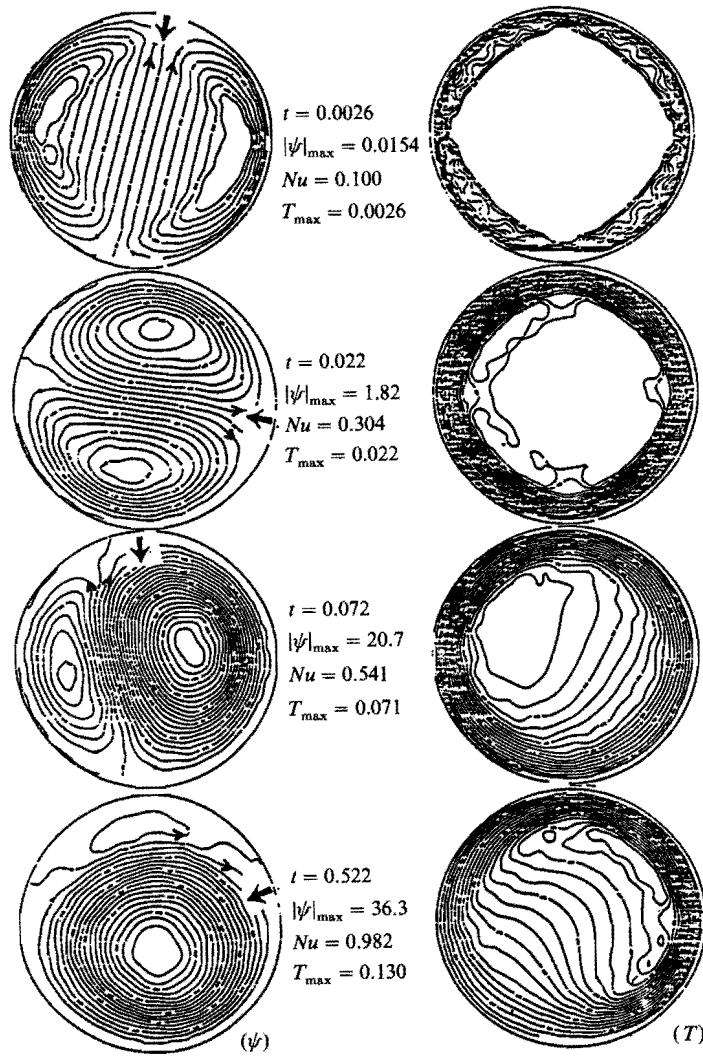
FIGURE 8. Transient evolution of normal-gravity driven convection when rotation is present. $Ra_g = 10^5$, $Re = 25$, and $Ra_r = 0$. The large arrows indicate the instantaneous direction of the clockwise-revolving normal gravity vector.

5.4. *Combined radial gravity, normal gravity and rotation*

Combined effects are now considered. It will be convenient to attribute radial gravity to rotation. As a consequence, the parameters Re and Ra_r are not independent with respect to the rotation rate, Ω. To isolate the rotation rate so that it appears only in Ra_r, we replace Re in (2) and (5) by

$$Re = \left(\frac{Ra_r}{Ra_g \Gamma}\right)^{\frac{1}{2}}, \tag{22}$$

where

$$\Gamma = \frac{\nu^2}{4 r_0^3 g_0}.$$

FIGURE 9. Quasi-stead
and rotation. Ra_g is va
indicate the instantan
$10^4 (Re = 78.4)$: $\psi = -$
(b) $Ra_g = 10^5 Re = 24.8$
$\zeta = -270 (270) 810$; p
(wall), $0.03 (0.015) 0.09$

Γ is a new paramete
frame gravity. The
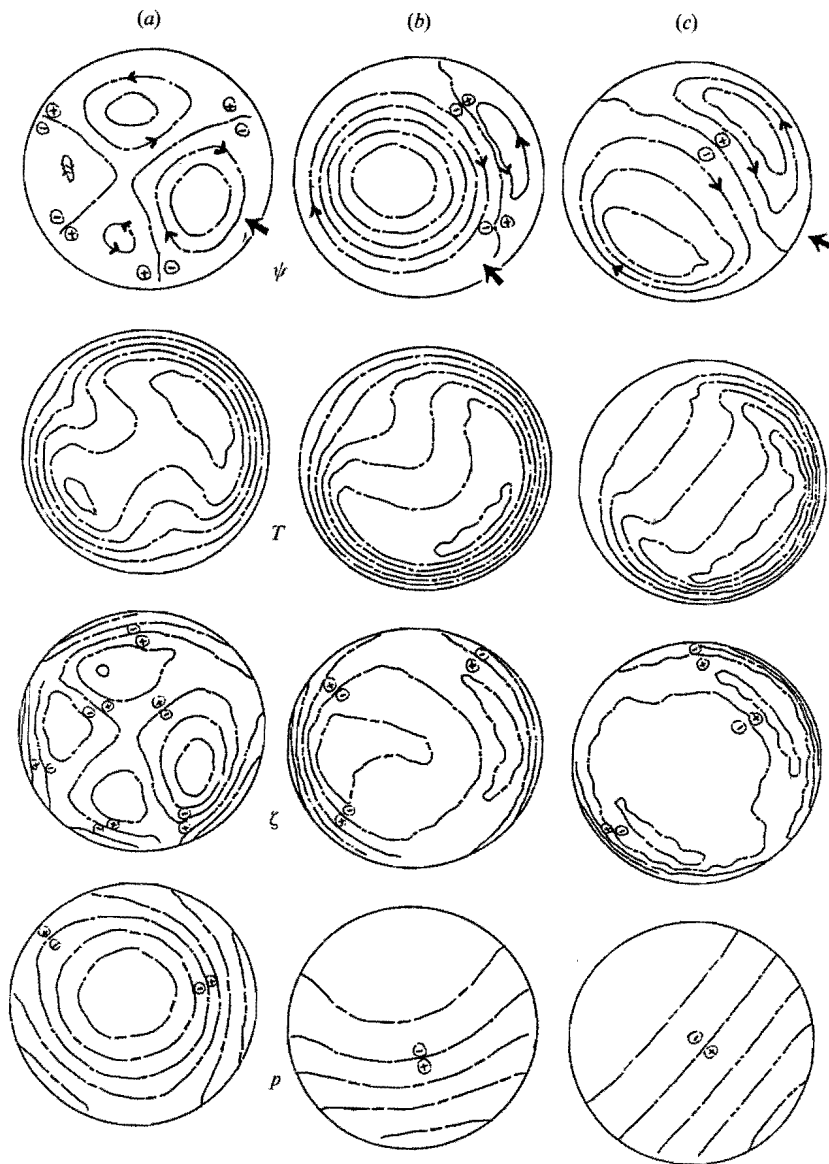independent parame

In the following
holding Γ fixed. S

FIGURE 9. Quasi-steady flows driven by the combined effects of radial gravity, normal gravity, and rotation. Ra_g is varied with $Ra_r = 10^5$. With Γ fixed, Re values are as noted. Large arrows indicate the instantaneous direction of the clockwise-revolving normal gravity vector. (a) $Ra_g = 10^4$ ($Re = 78.4$): $\psi = -6\,(3)\,6$; $T = 0\,(0.027)\,0.135$; $\zeta = -180\,(90)\,180$; $p = -12\,000\,(6000)\,18\,000$. (b) $Ra_g = 10^5$ $Re = 24.8$): $\psi = -30\,(6)\,0$ (primary cell); $\psi = 2.0$ (secondary cell); $T = 0\,(0.021)\,0.126$; $\zeta = -270\,(270)\,810$; $p = -24\,000\,(24\,000)\,72\,000$. (c) $Ra_g = 10^6$ ($Re = 7.8$): $\psi = -18\,(6)\,12$; $T = 0$ (wall), $0.03\,(0.015)\,0.09$ (other contours); $\zeta = -1800\,(900)\,1800$; $p = -15 \times 10^4\,(15 \times 10^4)\,45 \times 10^4$.

Γ is a new parameter involving the kinematic viscosity, cylinder radius, and inertial-frame gravity. The original four parameters listed in (4) are thus replaced by the four independent parameters Ra_r, Ra_g, Γ, and Pr.

In the following two subsections we consider the effect of normal gravity while holding Γ fixed. Steady and transient flows are examined (§§5.4.1 and 5.4.2,
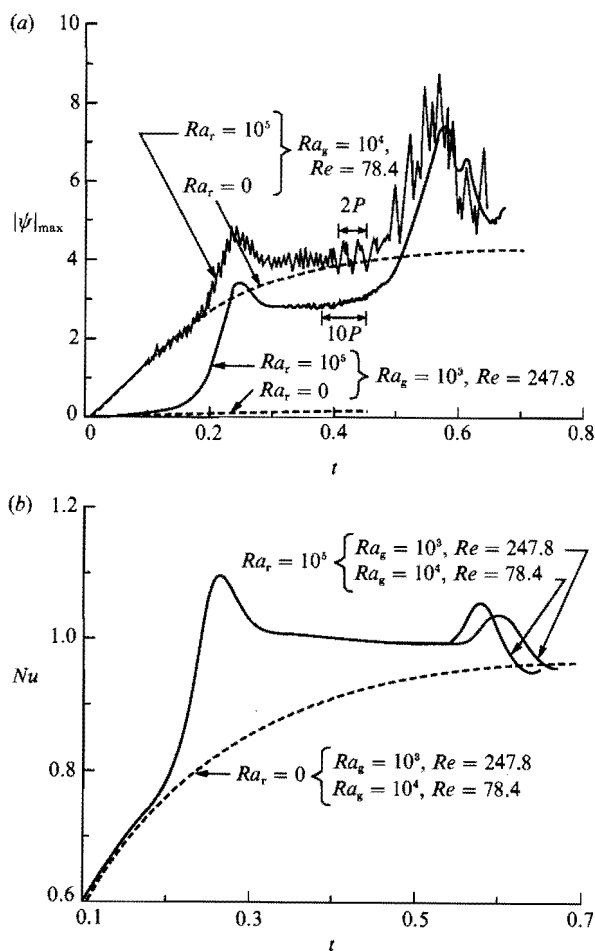
FIGURE 10. Temporal development when radial gravity, normal gravity, and rotational effects are present. The curve parameters are $Ra_g = 10^3$, 10^4 and $Ra_r = 0$, 10^5. P is the rotational period. (a) $|\psi|_{max}$. (b) Nu.

respectively). The parameters are $Ra_r = 10^5$, $10^3 \leqslant Ra_g \leqslant 10^6$, and $\Gamma = 1.628 \times 10^{-3}$. The associated Re range is $7.8 \leqslant Re \leqslant 247.8$. In the third subsection we examine the effects of variations in Γ (§5.4.3). Parameters are $Ra_r = 10^5$, $Ra_g = 10^4$, and $4.4 \times 10^{-4} \leqslant \Gamma \leqslant 1.628 \times 10^{-2}$ ($24.8 \leqslant Re \leqslant 150$). The case $\Gamma \to \infty$ ($Re = 0$) is also considered. To be consistent with the earlier presentations of results, parameter values will be expressed in terms of Ra_r, Ra_g, and Re where possible.

5.4.1. *Steady states*

Quasi-steady flows resulting from the combined effects of Ra_r and Ra_g are shown in figure 9. Columns (a), (b) and (c) respectively correspond to $Ra_g = 10^4$, 10^5, and 10^6, with $Ra_r = 10^5$. The flows are in the rotating frame and correspond to a time $t \approx 2.0$. The normal gravity vector (shown by large arrows) rotates clockwise; flows with similar orientations of the normal gravity vector are shown.

At $Ra_g = 10^4$ (figure 9a), the flow shows characteristic radial-gravity features and consists of a four-cell motion which is stationary in the rotating frame. The orientation of the four-cell structure is insensitive to the orientation of the normal
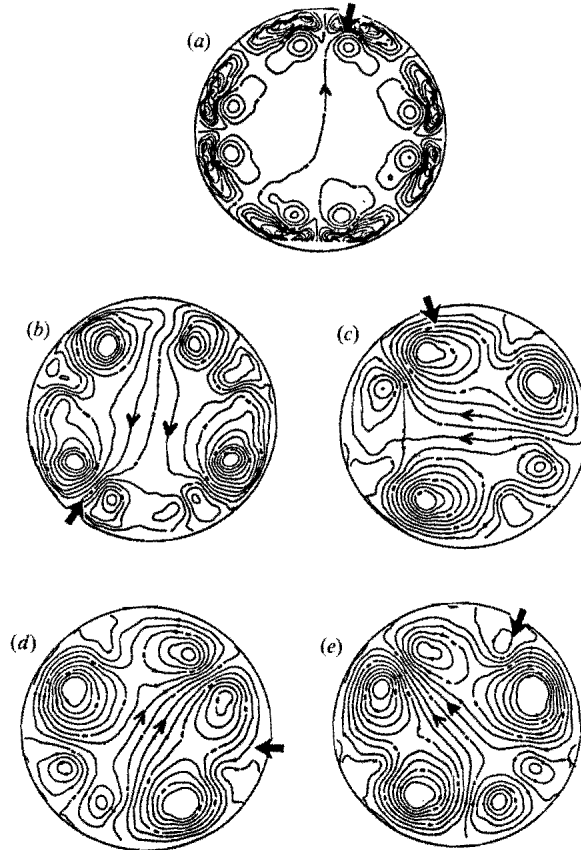
FIGURE 11. Transient stream function contours over a short time period when normal gravity and radial gravity are both important. $Ra_g = 10^3$, $Ra_r = 10^5$, and $Re = 247.8$. Convection driven by radial gravity dominates when $t > 0.15$. The normal gravity vector (shown by large arrows) revolves clockwise and the number of revolutions is η. (a) $t = 0.00022$, $\eta = 0.03$. (b) $t = 0.0043$, $\eta = 0.58$. (c) $t = 0.036$, $\eta = 4.9$. (d) $t = 0.060$, $\eta = 8.3$. (e) $t = 0.073$, $\eta = 10.1$.

gravity vector. However, individual cell flow rates vary as the normal gravity vector revolves. The four-cell structure is qualitatively similar to the radial gravity flow shown in figure 4(d) at a higher Ra_r value. At a lower value of Ra_g ($Ra_g = 10^3$ with $Ra_r = 10^5$, results not shown), a steady, two-cell, radial-gravity flow emerges which is essentially the same as the radial gravity flow shown in figure 4(c).

At $Ra_g = 10^5$ and 10^6 in figure 9(b–c), the influence of the rotating normal gravity vector is stronger. A two-cell flow emerges, with one cell enlarged with respect to the other, and rotates with the external normal gravity field. In the inertial frame, a near steady state is achieved at $Ra_g = 10^5$ (with a slight time dependence), and a true steady state at $Ra_g = 10^6$. At $Ra_g = 10^5$ and 10^6 in the rotating frame, the flows display periodic steady states, which are similar to those for combined normal gravity and rotation (e.g. at $t = 0.522$ in figure 8). In figure 9, stratification of the temperature field in the instantaneous direction of the normal gravity vector, and a relatively stagnant interior, are evident in those cases where normal gravity dominates. In all cases, isobars are generally perpendicular to the direction of the body force which causes the flows.
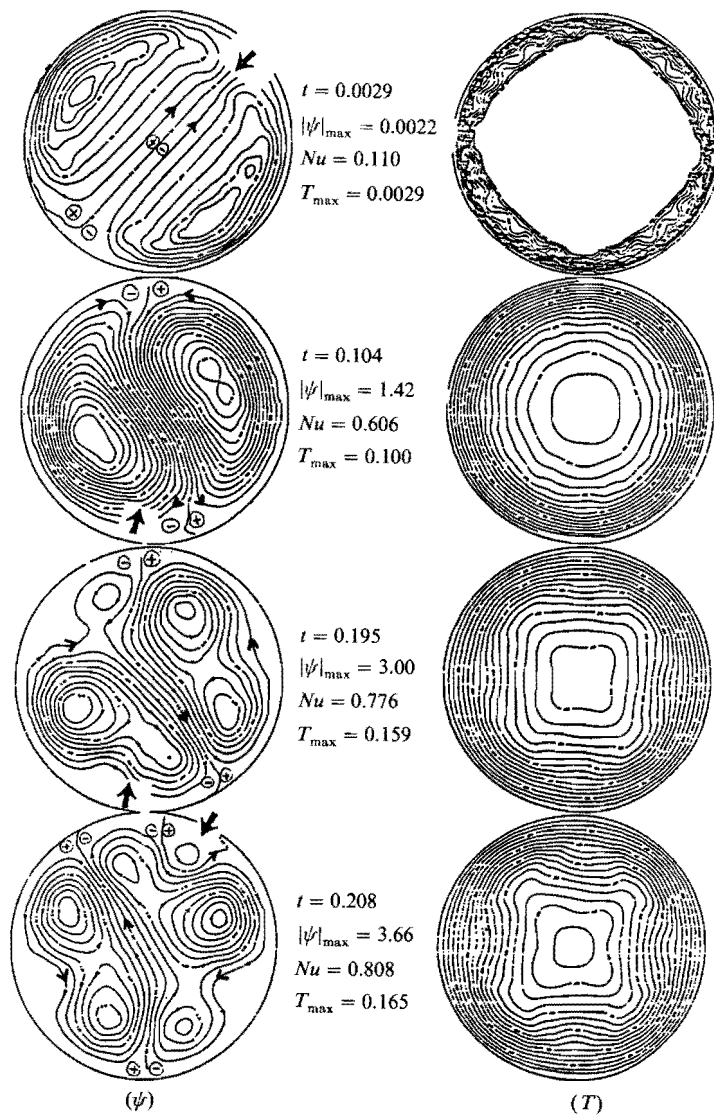
(ψ) $\qquad$ (T)

FIGURE 12. For caption see facing page.

5.4.2. *Transients*

The time evolution is shown in more detail in terms of $|\psi|_{max}$ and Nu in figure 10 (a,b), respectively. Curves are shown for $Ra_g = 10^3$ and 10^4, with and without the effect of radial gravity by using $Ra_r = 10^5$ and 0. (The results for $Ra_r = 0$ are from §5.3.)

In the absence of radial gravity (see dashed lines in figure 10), $|\psi|_{max}$ and Nu monotonically evolve to steady states for both Ra_g values, and the Nu transients are identical. When $Ra_r = 10^5$, the time evolution (solid lines) is not monotonic. Furthermore, the effect of radial gravity is manifested only after the conduction temperature profile is established ($t > 0.2$). This leads to large changes in $|\psi|_{max}$ and Nu at about that time. The $|\psi|_{max}$ transients clearly show a strong oscillation at

$t = 0.230$
$|\psi|_{max} = 4.30$
$Nu = 0.920$
$T_{max} = 0.172$

$t = 0.402$
$|\psi|_{max} = 5.62$
$Nu = 1.000$
$T_{max} = 0.144$

$t = 0.511$
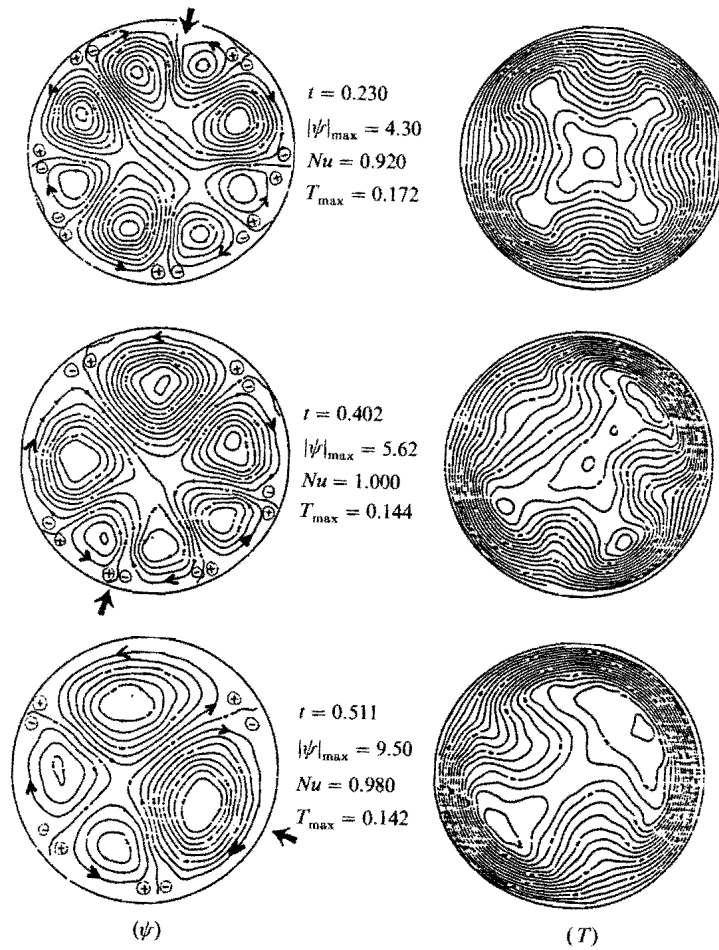$|\psi|_{max} = 9.50$
$Nu = 0.980$
$T_{max} = 0.142$

(ψ) (T)

FIGURE 12. Transient stream function (ψ) and temperature (T) contours over a time period when normal gravity and radial gravity are both important. $Ra_g = 10^4$, $Ra_r = 10^5$, and $Re = 78.4$. The normal gravity vector (shown by large arrows) revolves clockwise; the respective numbers of revolutions at the various times are $\eta = 0.13, 4.6, 8.5, 9.1, 10.0, 17.6$ and 22.3. The effects of normal gravity are stronger and of longer duration than for the transient in figure 11, but the final flow is also dominated by radial gravity.

$Ra_g = 10^4$ and a weak oscillation at $Ra_g = 10^3$. These oscillations are due to the interaction of the centrifugal (radial gravity) and normal gravity force fields. The oscillation periods correspond to the rotational period $P = 4\pi/Re\,Pr$, and contain higher harmonics. Time lines corresponding to multiples of P are shown in figure 10(a). We note in passing that the transients for $Ra_r = 10^5$, $Ra_g = 10^3$, $Re = 247.8$ are quite similar to those when radial gravity is dominant, i.e. for $Ra_r = 10^5$, $Ra_g = Re = 0$. The transients in figure 10 thus show regimes in which the two body forces are separately and jointly important.

Because of the lower critical Rayleigh number the effect of normal gravity, which is manifested in a two-cell convection pattern, often dominates the flow at short times when the two body forces are combined. This is especially true when $Ra_g > 10^3$ and $Ra_r = 10^5$. However, when $Ra_g = 10^3$ and $Ra_r = 10^5$, both forces make a comparable contribution to the amplitude of the flow for a short time, until $t \approx 0.1$,
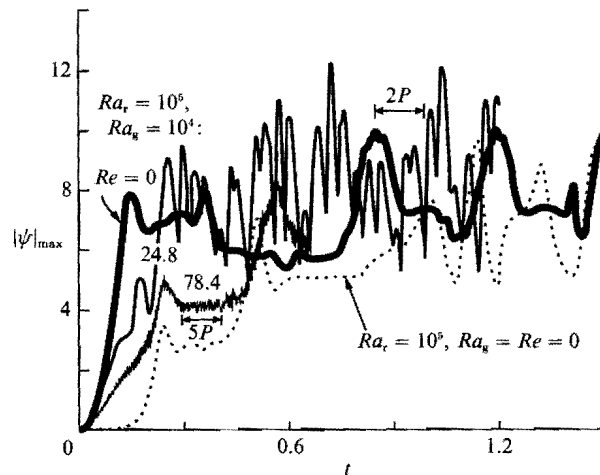
FIGURE 13. Temporal development of $|\psi|_{\max}$ for flows driven by radial gravity, normal gravity, and rotation. The solid lines correspond to $Ra_r = 10^5$ and $Ra_g = 10^4$ at various values of Re. P is the rotational period. The dotted line is for reference and corresponds to radial-gravity driven convection in the absence of normal gravity and rotation.

although the overall flow pattern itself is similar to that for radial gravity flows. Figure 11 shows the evolution of the flow pattern during the time in which both body forces are important. Only the streamlines are shown because heat transport is essentially by molecular diffusion. The effect of normal gravity is observed in the orientation of the convection pattern at $t = 0.00022$ in figure 11 (a). Figure 11 (e) corresponds to $t = 0.073$. Radial gravity effects are dominant when $t > 0.15$, and characteristic quantities such as $|\psi|_{\max}$, $T_{\max}$, $|\zeta|_{\max}$, etc., are those for radial gravity flows.

At $Ra_g = 10^4$ and $Ra_r = 10^5$, the effects of the two body forces are comparable through a longer part of the transient. The time-dependent contours of ψ and T are shown in figure 12. The flow pattern at short time consists of the two-cell normal-gravity mode oriented in the direction of the normal gravity vector. As the conduction temperature field is established the effect of radial gravity appears, and a multicellular flow in the rotating frame results.

The common observation in the flow fields of figures 11 and 12 is that the two normal-gravity cells at early times are distorted, looking like 'wavetrains', as they encircle two or three radial-gravity cells that circulate in the same direction. Cells with reverse circulations appear in-between the main cells to reduce shear. Further, a few of the flows in figure 12 (e.g. at $t = 0.230$) resemble those associated with baroclinic waves in an internally-heated annulus with vanishing inner-cylinder radius (Hide & Mason 1970). An explanation for this can be found in the baroclinicity of the two systems.

5.4.3. *Effect of Γ*

The effects of variations in Γ are discussed in this section for $Ra_r = 10^5$, $Ra_g = 10^4$, and $4.4 \times 10^{-4} \leqslant \Gamma \leqslant 1.628 \times 10^{-2}$. The limit $\Gamma \to \infty$ is also considered. With Ra_r/Ra_g fixed, the range of Γ is equivalent to studying the effect of Re for $0 \leqslant Re \leqslant 150$.

Time traces of $|\psi|_{\max}$ are shown in figure 13 for three values of Re (see solid lines for $Re = 0$, 24.8, and 78.4). For $Re = 0$, the fully developed flow is time periodic. For

$Re > 0$, normal gravity effects induce oscillations with the period, P, of the rotating gravity vector. Multiples of P are shown with time lines in figure 13; for $Re = 0$, however, P is infinite. Flow strength and heat transport reach a maximum near $Re \approx 25$, and decrease on either side of this value. At $Re = 24.8$ in figure 13, the mean and fluctuating values of $|\psi|_{max}$ have their maximum values. At higher Re, both the period and amplitude of the rotation-induced fluctuations decrease. Furthermore, when $Re > 78$, the flows are only slightly stronger than those for radial gravity alone, as shown by referring to the dotted line for $Ra_r = 10^5$, $Ra_g = Re = 0$. The foregoing effects of Re are similar to those observed for normal gravity flows with rotation (§5.3), but the present transient interactions are much stronger.

6. Summary

For an internally-heated horizontal cylinder rotating about its axis, and subjected to radial and/or normal gravity, the major findings are:

1. The radial-gravity rest state becomes unstable at $Ra_{r,c} = 13738$ in a bicellular motion with azimuthal wavenumber one. For flows driven by normal gravity, the preferred motion also corresponds to azimuthal wavenumber one, but is aligned with the external gravity vector. Although motion in the latter case occurs for all $Ra_g > 0$, temperatures do not depart significantly from the conduction field until $Ra_g > 400$.

2. Flows driven by radial gravity are relatively more efficient at transporting heat than flows driven by normal gravity (figure 3).

3. Time-dependent convective mode switching and cell-size adjustment were observed in transient, two-dimensional calculations (figure 5) for flows driven by radial gravity for Ra_r values up to $70Ra_{r,c}$. Initial conditions play a minor role in determining the final flow field except perhaps in the azimuthal orientation of the cells, which is otherwise arbitrary. This result is at variance with reports by Weir (1976) on axisymmetric convection in a self-gravitating sphere. However, convective mode switching and cell-size adjustment may not arise when axisymmetry is assumed as in Weir (1976) or Hsui *et al.* (1972).

4. The two cells produced by normal gravity in an inertial frame tend to coalesce into a single cell when observed in a rotating frame (figure 8). The secondary cell diminishes with increasing Re.

5. Complex time-dependent flows with large shear and complicated wave motions are observed when the effects of the two body forces are comparable.

6. For fixed Ra_r and Ra_g, there is an optimum Re (non-zero) that gives the maximum effect of normal gravity, and, at sufficiently large Re, the flow is due to radial gravity. Thus, when Ra_r is small and Re much larger than the optimum value, the temperature field approaches pure conduction and the flow field approaches solid-body rotation when observed in an inertial frame.

REFERENCES

BUSSE, F. H. 1986 Asymptotic theory of convection in a rotating, cylindrical annulus. *J. Fluid Mech.* **173**, 545–556.

CHEN, M. M. & WHITEHEAD, J. A. 1968 Evolution of two-dimensional periodic Rayleigh convection cells of arbitrary wave-numbers. *J. Fluid Mech.* **31**, 1–15.

DANIELS, P. G. 1984 Roll-pattern evolution in finite-amplitude Rayleigh–Bénard convection in a two-dimensional fluid layer bounded by distant sidewalls. *J. Fluid Mech.* **143**, 125–152.

FUSEGI, T., FAROUK, B. & BALL, K. S. 1986 Mixed-convection flows within a horizontal concentric annulus with a heated rotating inner cylinder. *Numer. Heat Transfer* **9**, 591–604.

GOLLUB, J. P., MCCARRIAR, A. R. & STEINMAN, J. F. 1982 Convective pattern evolution and secondary instabilities. *J. Fluid Mech.* **125**, 259–281.

GREENSPAN, H. P. 1969 *The Theory of Rotating Fluids*. Cambridge University Press.

GRESHO, P. M., LEE, R. L. & SANI, R. L. 1980 On the time-dependent solution of the incompressible Navier–Stokes equation in two and three dimensions. *Recent Advances in Numerical Methods in Fluids* (ed. C. Taylor & K. Morgan), vol. 1. Swansea, UK: Pineridge Press Ltd.

HIDE, R. 1967 Theory of axisymmetric thermal convection in a rotating fluid annulus. *Phys. Fluids* **10**, 56–68.

HIDE, R. & MASON, P. J. 1970 Baroclinic waves in a rotating fluid subject to internal heating. *Phil. Trans. R. Soc. Lond.* A **268**, 201–232.

HIDE, R. & MASON, P. J. 1974 Sloping convection in a rotating fluid. *Adv. Phys.* **24**, 47–100.

HSUI, A. T., TURCOTTE, D. L. & TORRANCE, K. E. 1972 Finite amplitude thermal convection within a self-gravitating fluid sphere. *Geophys. Fluid Dyn.* **3**, 35–44.

HUTCHINS, J. & MARSCHALL, E. 1989 Pseudosteady-state natural convection heat transfer inside spheres. *Intl J. Heat Mass Transfer* **32**, 2047–2053.

JOSEPH, D. D. 1966 Nonlinear stability of the Boussinesq equations by the energy method. *Arch. Rat. Mech. Anal.* **22**, 163–184.

JOSEPH, D. D. & CARMI, S. 1969 Stability of Poiseuille flow in pipes, annuli and channels. *Q. Appl. Maths* **26**, 575–599.

LADEINDE, F. 1986 Design of a dual rotating system for thermal processing of canned fluid foods. M. Engng Rep. Sibley School of Mechanical and Aerospace Engineering, Cornell University, Ithaca, New York, USA.

LADEINDE, F. 1988 Studies on thermal convection in self-gravitating and rotating horizontal cylinders in a vertical external gravity field. PhD thesis, Sibley School of Mechanical and Aerospace Engineering, Cornell University, Ithaca, New York, USA, 346 pp.

LADEINDE, F. & TORRANCE, K. E. 1990 Galerkin finite element simulation of convection driven by rotation and gravitation. *Intl J. Numer. Meth. Fluids* **10**, 47–77.

LEE, T. S. 1984 Numerical experiments with laminar fluid convection between concentric and essentric heated rotating cylinders. *Numer. Heat Transfer* **7**, 77–87.

LIN, Y. S. & AKINS, R. G. 1986 Pseudo-steady-state natural convection heat transfer inside a vertical cylinder. *Trans. ASME* C: *J. Heat Transfer* **108**, 310–316.

LOPEZ, A. 1981 *A Complete Course in Canning. Book 1. Basic Information on Canning*. The Canning Trade, Baltimore, Maryland, USA.

MORI, Y. & NAKAYAMA, W. 1967 Forced convective heat transfer in a straight pipe rotating about a parallel axis (laminar region). *Intl J. Heat Mass Transfer* **10**, 1179–1194.

OSTRACH, S. 1972 Natural convection in enclosures. *Adv. Heat Transfer* **8**, 161–227.

RANDRIAMAMPIANINA, A., BONTOUX, P. & ROUX, B. 1987 Ecoulements induits par la force gravifique dans une cavité cylindrique en rotation. *Intl J. Heat Mass Transfer* **30**, 1275–1292.

SABZEVARI, A. & OSTRACH, S. 1974 Experimental studies of natural convection in a horizontal cylinder. In *Fifth Intl Heat Transfer Conf. Tokyo, Japan*, vol. 8, pp. 100–104.

TAKEUCHI, M. & CHENG, K. C. 1976 Transient natural convection in horizontal cylinders with constant cooling rate. *Wärme-und-Stoffübertragung* **9**, 215–225.

VAHL DAVIS, G. DE 1983 Natural convection of air in a square cavity: a benchmark numerical solution. *Intl J. Numer. Meth. Fluids* **3**, 249–264.

VAN SANT, J. H. 1969 Free convection of heat-generating liquids in a horizontal pipe. *Nucl. Engng Design* **10**, 349–355.

WEIR, A. D. 1976 Axisymmetric convection in a rotating sphere. Part I. Stress free surface. *J. Fluid Mech.* **75**, 49–79.

WOODS, J. L. & MORRIS, W. D. 1980 A study of heat transfer in a rotating cylindrical tube. *Trans. ASME* C: *J. Heat Transfer* **102**, 612–616.

YANG, H. Q., YANG, K. T. & LLOYD, J. R. 1988 Rotational effects on natural convection in a horizontal cylinder *AIChE J.* **34**, 1627–1633.